Chapter 6

The Analysis of Temporary Temperature Field and Phase Transformations in One-Side Butt-Welded Steel Flats

Jerzy Winczek

Additional information is available at the end of the chapter

http://dx.doi.org/10.5772/63994

Abstract

In this chapter, the welding method applied for modelling the temperature field and phase transformations is presented. Three-dimensional and temporary temperature field for butt welding with thorough penetration was determined on the basis of analytical methods of an integral transformation and Green's function. Structural changes of heating and cooling, proceeding in a weld (in the heat-affected zone), were described using the existing formulations of phase transformations. Considerations were illustrated by an example, for which analysis of temperature fields, developed by a moving heat source, and calculations of the distribution of particular phases (structures) were carried out. Metallographic studies of the butt joints, which were arc welded under a flux, were carried out in the empirical part of this work. Their results enabled the verification of the numerical simulation results of the phase transformations.

Keywords: butt-welded joint, temperature field, HAZ, phase transformations, numerical modelling, metallographic examination

1. Introduction

Welding is characterised by many specific features associated with variable temperatures and variable physical and mechanical properties of the welding material. The moving heat source, characteristic of welding, partial melts the joint surface and fuses an electrode. The electrode fills a joint space with liquid metal. Hence, welding elements are subjected to varying temperature ranges, that is, from ambient to that of a liquid metal.

Crystallisation and solidification, segregation of alloy elements and solutes and structural changes caused by intensive cooling occur extensively. Thermal and mechanical states and microstructure directly state about the quality of the welding joint.

Modelling the temperature field during welding was first initiated by Rosenthal [1] and Rykalin [2], who supposed the point and linear models of heat source, respectively. The adoption of a point heat source, as in the above-mentioned studies, yields results with respect to the points located near the centre of the weld, which are significantly different from the actual temperature values. Therefore, Eagar and Tsai [3] proposed a two-dimensional (2D) Gaussian-distributed heat source model and developed a solution of temperature field in a semi-infinite steel plate. Subsequently, Goldak et al. [4] introduced a double ellipsoidal three-dimensional heat source model. There are two ways of modelling the temperature field during welding: analytical [5–14] and numerical (the finite difference methods, infinitesimal heat balances and finite element method) [15–30]. The welding methods and types of joints can be studied through these approaches [6, 20, 21, 31–33]. The construction of numerical models with heightening complexity allows more essential factors for the exact description of the structural changes in the welded steel.

2. Temperature field in the butt-welded joint with thorough penetration

Welding is characterised by an application of the movable, concentrated heat source, which in turn makes the temperature field movable in time and space:

$$T = T(r,t) = T(x,y,z,t) \tag{1}$$

Studies are being conducted to develop models of temperature field. Such models should have a real-time shape and temperature gradients based on the geometrical dimension of the welding element and also time. Referring to the formulated problem, the solution of heat equation for isotropic medium is essential to determine a temporary temperature field:

$$\nabla^2 T(r,t) = \frac{1}{a}\frac{\partial}{\partial t}T(r,t) - \frac{f(r,t)}{\lambda} \tag{2}$$

where T(r,t) is temperature at r position at t time, a is the coefficient of temperature compensation, λ thermal conductivity and f(r,t) supplied energy per volume and time unit.

Analytical method, proposed by Geissler and Bergmann [34, 35], was chosen to solve this differential equation. A short description of the method, described in detail in the above-mentioned studies, is presented below.

The following assumptions were accepted in the calculations:

– quantities characterising the material properties, such as thermal conductivity, temperature compensation and thermal capacity, are constant (independent from temperature),

http://dx.doi.org/10.5772/63994

– heat waste by convection and radiation is negligible,

– reciprocal interaction of temperature field and phase changes is not taken into account,

– heat of fusion is not taken into consideration.

A sample with thickness of D and width of $B_1 + B_2$, heated by the movable welding heat source, which is displaced at velocity v along the x-axis (**Figure 1**), is an illustration of the below consideration.

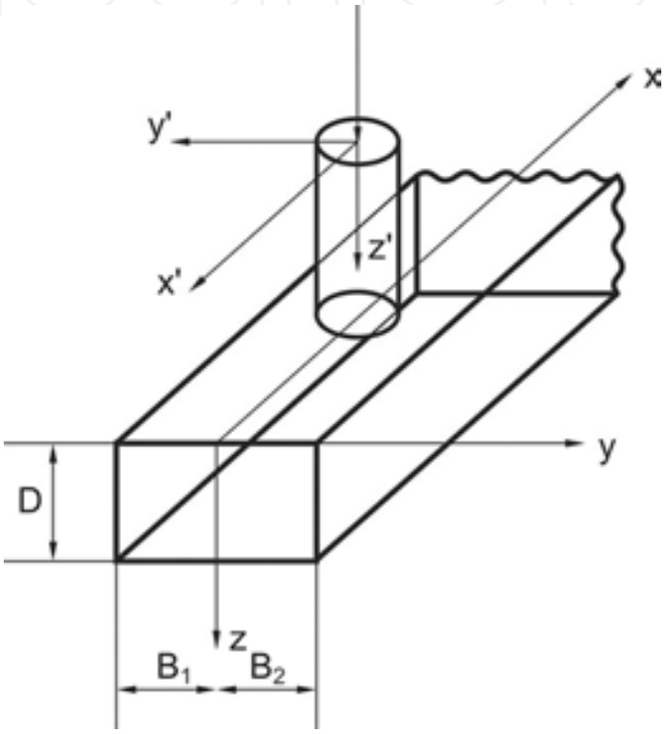

Figure 1. Schematic of heating of a steel sample using welding heat source.

According to Geissler and Bergmann [34, 35], the solution of Eq. (2) can be written as a superposition of Green's function. This leads to the following convolution of integrals as a general expression of temperature

$$T(r,t) = \frac{a}{\lambda}\int_0^t \iiint f(r',t')\,G(|r-r'|,t-t')\,dx'dy'dz'dt' \tag{3}$$

where $r(x,y,z)$ is a vector pointing the place on the sample, while $r' = (x',y',z')$ determines the source position. Green's function G describes the temperature field in the point of material defined by r in time t. It is caused by a point heat source acting in the r' position and at $t' < t$ time. G depends on the geometry of the sample and can be determined by transformation method, while f defines the cross-section of the welding heat source.

A three-dimensional temperature field with the possibility of acceptance of different geometries of samples as well as the shape of the heat source can be determined from Eq. (3).

In the case of the Gauss model of heat source, we have

$$f(x,y)=\frac{P}{2\pi R^2}\exp\left(-\frac{x^2+y^2}{2R^2}\right),-\infty<x<\infty,-\infty<y<\infty, \tag{4}$$

where the power of source is denoted by P and determined for R radius and corresponds to 1/e of its peak value (**Figure 2**).

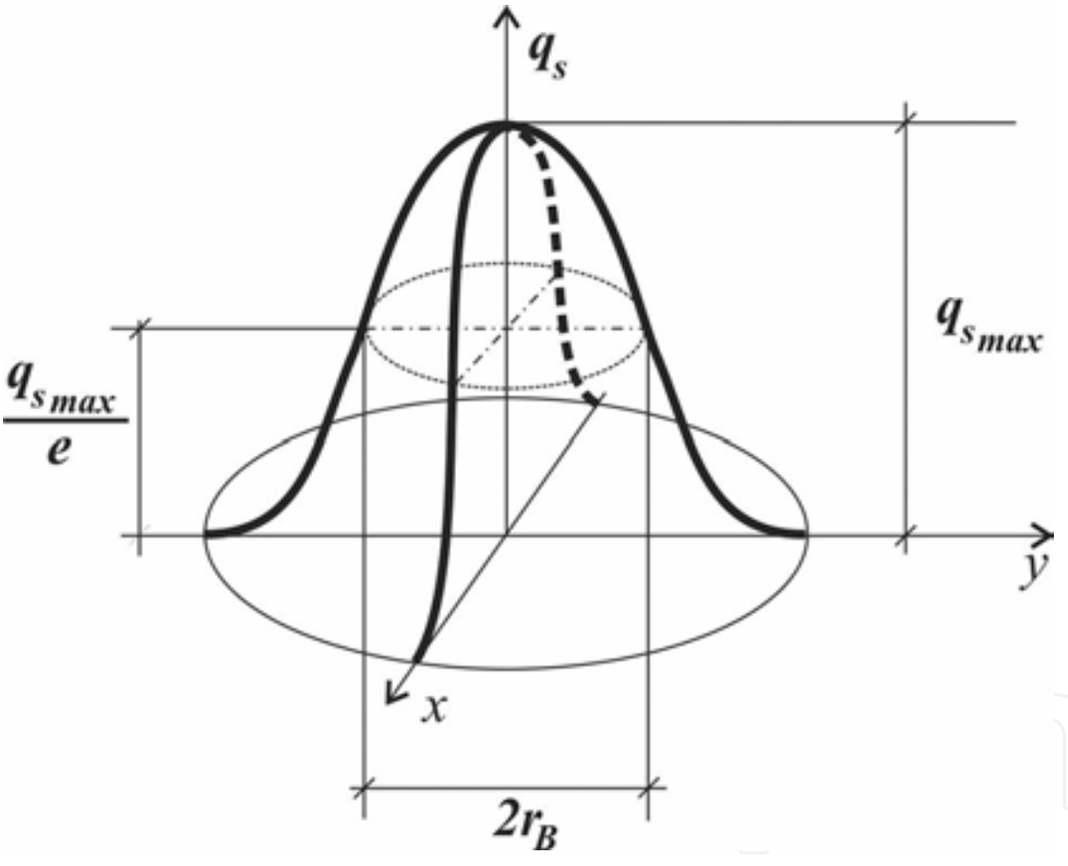

Figure 2. Gauss distribution of power of the heat source.

An infinitely long bar with the above-mentioned dimensions of cross-section was accepted in the considered example (**Figure 1**).

This can be written in the Cartesian coordinate system as follows:

$$-\infty<x<\infty,-B_1\le y\le B_2,0\le z\le D \tag{5}$$

http://dx.doi.org/10.5772/63994

Boundary conditions defining the surface and Green's function were taken from the study by Carslaw and Jaeger [36]. Green's function takes the following form:

$$G\left(\left|r-r'\right|,t-t'\right)=G_{(x)}\left(x-x',t-t'\right)G_{(y)}\left(y-y',t-t'\right)G_{(z)}\left(z,t-t'\right) \tag{6}$$

$$G_{(x)}=\left[4\pi a\left(t-t'\right)\right]^{-1/2}\exp\left(-\frac{\left(x+v\left(t_0-t'\right)-x'\right)^2}{4a\left(t-t'\right)}\right) \tag{7}$$

$$\begin{aligned}G_{(y)}=&\left[4\pi a\left(t-t'\right)\right]^{-1/2}\times\left[\sum_{n=-\infty}^{\infty}\exp\left(-\frac{\left[y-y'-2n\left(B_2+B_1\right)\right]^2}{4a\left(t-t'\right)}\right)\right.\\&+\sum_{n=1}^{\infty}\exp\left(-\frac{\left[y-y'-2nB_2-2\left(n-1\right)B_1\right]^2}{4a\left(t-t'\right)}\right)\\&\left.+\sum_{n=1}^{\infty}\exp\left(-\frac{\left[y-y'+2nB_1+2\left(n-1\right)B_2\right]^2}{4a\left(t-t'\right)}\right)\right]\end{aligned} \tag{8}$$

$$G_{(z)}=\left[4\pi a\left(t-t'\right)\right]^{-1/2}\sum_{n=-\infty}^{\infty}\exp\left(-\frac{\left(z-2nD\right)^2}{4a\left(t-t'\right)}\right) \tag{9}$$

where n is the transformation number of the source.

The relationship of movement of the welding heat source to the welding element is included in $G(x)$ function. Because a flat model of heat source was assumed, the z' coordinate is not present in $G(z)$ function. The coordinate systems connected with the heat source and welding material coincide with t_0 time. Considering that the shape of the heat source is independent of time, z' is dependent on f and G is eliminated; a modified integral to count temperature profile is thus obtained:

$$T\left(r,t\right)=\frac{a}{\lambda}\int_0^t\iint f\left(x',y'\right)G\left(\left|r-r'\right|,t-t'\right)dx'dy'dt' \tag{10}$$

z' integral is removed in comparison to Eq. (3).

Temperature distribution can be calculated after substituting Green's function and Eq. (4) into Eq. (10). The integral over a range of variables can be evaluated, which yields the following result:

$$T(x,t)=\frac{\eta P}{2\pi\rho Cp}\int_0^t u(t,t')\sum_{n=-\infty}^{\infty}\exp\left(-\frac{(z-2nD)^2}{4a(t-t')}\right)$$
$$\times\left\{\sum_{n=-\infty}^{\infty}\exp\left(-\frac{\left(x+v(t_0-t'))\right)^2+(y-4nB)^2}{2R^2+4a(t-t')}\right)F_1(y)\right.$$
$$+\sum_{n=-\infty}^{\infty}\exp\left(-\frac{\left(x+v(t_0-t'))\right)^2+(y-4nB)^2}{2R^2+4a(t-t')}\right)F_2(y)$$
$$\left.+\sum_{n=-\infty}^{\infty}\exp\left(-\frac{\left(x+v(t_0-t'))\right)^2+(y-4nB)^2}{2R^2+4a(t-t')}\right)F_3(y)\right\}dt'+T_0 \tag{11}$$

where

$$u(t,t')=\frac{1}{2\sqrt{\pi a(t-t')}\left(R^2+2a(t-t')\right)} \tag{12}$$

$$F_{1(y)}=erf\left(\sqrt{\frac{R^2+2a(t-t')}{4aR^2(t-t')}}\left(B_2-\frac{R^2(y-4nB)}{R^2+2a(t-t')}\right)\right)+$$
$$-erf\left(\sqrt{\frac{R^2+2a(t-t')}{4aR^2(t-t')}}\left(-B_1-\frac{R^2(y-4nB)}{R^2+2a(t-t')}\right)\right) \tag{13}$$

$$F_{2(y)}=erf\left(\sqrt{\frac{R^2+2a(t-t')}{4aR^2(t-t')}}\left(B_2-\frac{R^2(y-2(2n-1)B)}{R^2+2a(t-t')}\right)\right)+$$
$$-erf\left(\sqrt{\frac{R^2+2a(t-t')}{4aR^2(t-t')}}\left(-B_1-\frac{R^2(y-2(2n-1)B)}{R^2+2a(t-t')}\right)\right) \tag{14}$$

$$F_{3(y)}=erf\left(\sqrt{\frac{R^2+2a(t-t')}{4aR^2(t-t')}}\left(B_2-\frac{R^2(y+2(2n-1)B)}{R^2+2a(t-t')}\right)\right)+$$
$$-erf\left(\sqrt{\frac{R^2+2a(t-t')}{4aR^2(t-t')}}\left(-B_1-\frac{R^2(y+2(2n-1)B)}{R^2+2a(t-t')}\right)\right) \tag{15}$$

http://dx.doi.org/10.5772/63994

3. Kinetics of phase transformations in a solid state

Heating processes of steel lead to the transformation of a primary structure into austenite, while cooling leads to the transformation of austenite into ferrite, pearlite, bainite and martensite. Structural changes of a welded joint, connected with its cooling (also with hardening), develop heterogeneous image of material structure, which influences the state of stress after welding. The zone with a yield point lesser or greater than that of an indigenous material can occur in the welded joint.

Mechanical properties of the joint mostly depend on the type of welding material (its primary structure and chemical constitution of steel) and the characteristics of heat cycles accompanying welding. Temperature levels attained during heating, the hold time at a particular temperature and velocity of cooling in the 800–500°C range determine the type of structure present in the joint during and after welding.

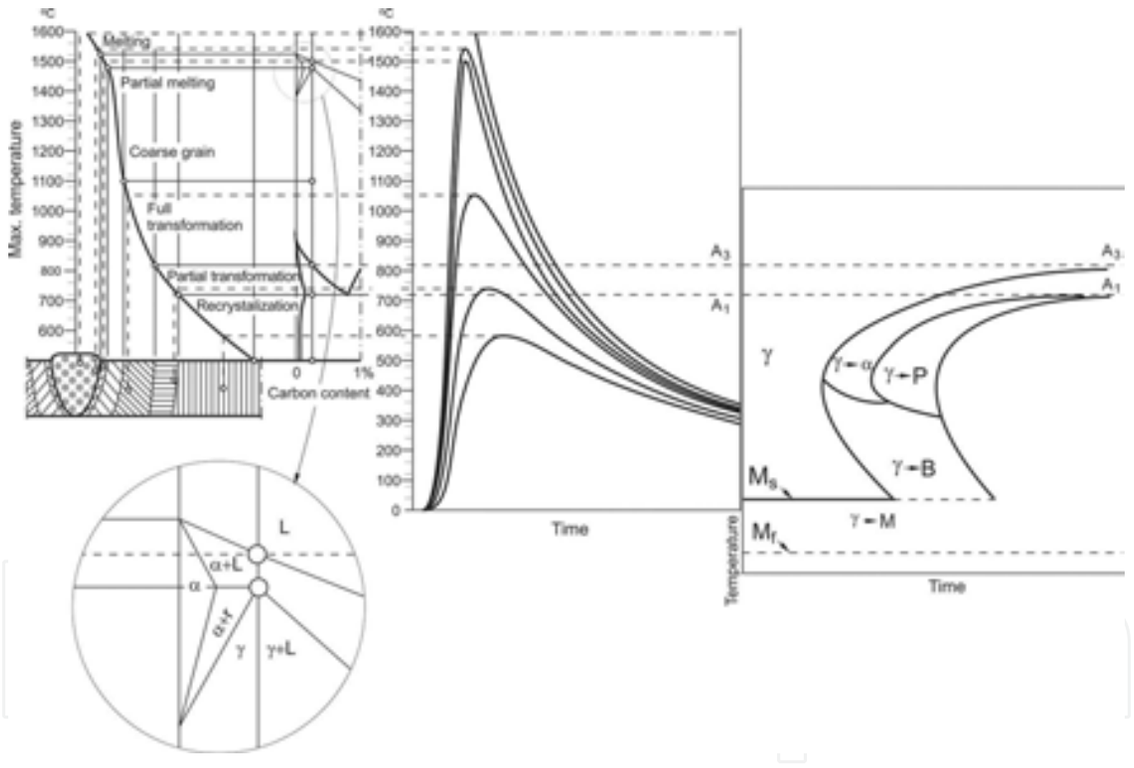

Figure 3. Characteristic structural areas of a welded joint, depending on the temperature and the share of the carbon in the steel.

Figure 3 shows the distribution characteristics of the weld joint zone of structural carbon steel [37] with a schematic of the fragment of an iron-carbon system and fragment of the TTT-welding diagram. Together, it is categorised into the following zones:

– fusion zone, which undergoes a thorough penetration and is characterised by the dendritic structure of solidification,

- partial joint penetration, where material is in a semi-fluid state and creates the border between the melted material and the material being converted into austenite,
- the course-grained structure, the so-called overheating zone,
- proper transformation, where perfect conversion of primary structure into austenite occurs,
- partial transformation between temperature A_1 at the beginning of austenisation and A_3 at the end of austenisation, where only a part of the structure changes into austenite,
- recrystallisation.

Several studies have focused on the description and numerical modelling of steel phase transformations. These studies have been reviewed by Rhode and Jeppson [38].

The type of a newly created phase depends heavily on the kinetics of heating and cooling processes. Kinetics of those processes is described by Johnson-Mehl-Avrami's and Kolomogorov's (JMAK) rules [39]. The amount of austenite ϕ_A created while heating the ferrite-pearlitic steel is therefore defined according to the following formula:

$$\varphi_A(T) = \sum_j \varphi_j^0 \left(1 - \exp\left(-b_j(T) t^{n_j(T)}\right)\right) \tag{16}$$

where ϕ_j^0 constitutes an initial share of ferrite ($j \equiv F$), pearlite ($j \equiv P$) and bainite ($j \equiv B$), while constants b_j and n_j are determined using conditions of the beginning and the end of transformation:

$$n_j = \frac{\ln\left(\ln(0.99)\right)}{\ln\left(A_1 / A_3\right)}, b_j = \frac{0.01 n_i}{A_1} \tag{17}$$

In welding processes, the volume fractions of particular phases during cooling depend on the temperature, cooling rate, and the share of austenite (in the zone of incomplete conversion $0 \le \phi_A \le 1$). In a quantitative perspective, the progress of phase transformation during cooling is estimated using additivity rule by voluminal fraction ϕ_j of the created phase, which can be expressed analogically in Avrami's formula [40] by equation:

$$\varphi_j(T,t) = \varphi_A \varphi_j^{\max} \left\{1 - \exp\left[b_j\left(T\left(v_{8/5}\right)\right) t(T)^{n\left(T\left(v_{8/5}\right)\right)}\right]\right\} \tag{18}$$

where φ_j^{max} is the maximum volumetric fraction of phase j for the determined cooling rate estimated on the basis of the continuous cooling diagram (**Figure 4**), while the integral volumetric fraction equals to:

http://dx.doi.org/10.5772/63994

$$\sum_{j=1}^{k} \varphi_j = 1 \tag{19}$$

and k denotes the number of structural participations.

The quantitative description of dependence of the material structure and quality on temperature and transformation time of overcooled austenite during surfacing is made using the time-temperature-transformation diagram during continuous cooling, which combines the time of cooling $t_{8/5}$ (time when material stays within the range of temperature between 500 and 800°C, or the velocity of cooling ($v_{8/5}$ – (800 – 500)/$t_{8/5}$) and the temperature with the progress of phase transformation (**Figure 4**). Those diagrams are called TTT–welding diagrams.

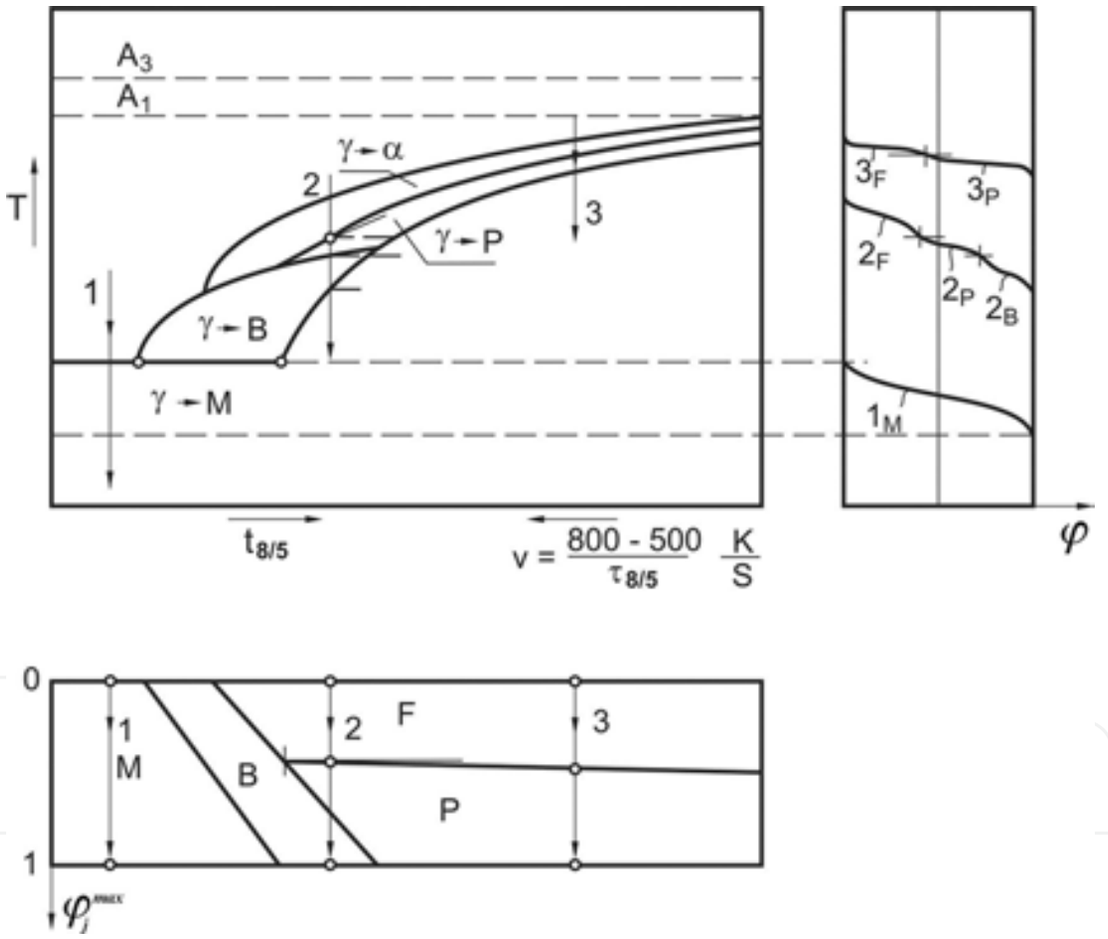

Figure 4. Scheme of phase changes of overcooled austenite depending on cooling velocity within temperature range 800–500°C.

Quantitatively, the progress of phase transformation is estimated by volumetric fraction ϕ_j of the created phase, where i denotes ferrite ($j \equiv F$), pearlite ($j \equiv P$), bainite ($j \equiv B$) or martensite ($j \equiv M$). The volumetric fraction ϕ_j of the created phase can be expressed using a formula given in Eq. (27), wherein time t is replaced with a new independent variable, temperature T [41]:

$$\varphi_j = \varphi_A \varphi_j^{\max} \left(1 - \exp\left(-b_j T^{n_j}\right)\right) + \varphi_j^0 \tag{20}$$

where

$$n_j = \frac{\ln\left(\ln\left(1-\varphi_j^s\right) / \ln\left(1-\varphi_j^f\right)\right)}{\ln\left(T_j^s / T_j^f\right)}, b_j = \frac{n_j\left(1-\varphi_j^f\right)}{T_j^s} \tag{21}$$

$$\frac{\varphi_j^s}{\varphi_j^{\max}} = 0,01, \frac{\varphi_j^f}{\varphi_j^{\max}} = 0,99 \tag{22}$$

ϕ_j^0 is the volumetric participation of *j*-th structural component, which has not been converted during austenitisation; $T_j^s = T_j^s(v_{8/5})$ and $T_jf = T_j^f(v_{8/5})$ are, respectively, the initial and final temperature of phase transformation of this component.

The fraction of martensite formed below the temperature M_s is calculated using the Koistinen-Marburger formula [42, 43]:

$$\varphi_M\left(T\right) = \varphi_A / \varphi_M^{\max}\left\{1 - \exp\left[-\mu\left(M_s - T\right)\right]\right\}, \mu = -\frac{\ln\left(\varphi_M^{\min} = 0.1\right)}{M_s - M_f} \tag{23}$$

where ϕ_m denotes the volumetric fraction of martensite; M_s and M_f denote the initial and final temperature of martensite transformation, respectively; T is the current temperature of the process.

4. Thermal and phase transformation strains

Changes in temperature during welding cause deformations associated with the thermal expansion and deformation of the material resulting from the structural phase transformation. Deformation during the whole thermal cycle is the total deformation created during heating and cooling [44]:

$$\varepsilon\left(x,y,z,t\right) = \varepsilon^H + \varepsilon^C \tag{24}$$

where ε^{H} and ε^C denote the thermal and phase transformation strains during heating and cooling, respectively.

Heating leads to an increase in the material volume, while transformation of the initial structure (ferritic, pearlitic or bainitic) in austenite causes shrinkage which is associated with

http://dx.doi.org/10.5772/63994

different densities of the given structures. Then, the strain caused during heating is calculated as follows:

$$\varepsilon^{H} = \varepsilon^{Th} - \varepsilon^{Trh} \tag{25}$$

where ε^{Th} is the strain caused by thermal expansion of the material:

$$\begin{aligned}\varepsilon^{Th} = \sum_{i=A,P,F,B,M} & (\alpha_i \varphi_{i0} (T - T_0) H(T_{A_1} - T) + \alpha_i \varphi_i (T - T_{A_1}) H(T_{A_3} - T) H(T - T_{A_1}) + \\ & + \alpha_A (T - T_{A_3}) H(T - T_{A_3}))\end{aligned} \tag{26}$$

while ε^{Trh} is the phase transformation strain during heating:

$$\varepsilon^{Trh} = \sum_{i=P,F,B,M} \varphi_i \gamma_{iA} \tag{27}$$

where γ_{iA} is the structural strain of the i-th structure in austenite, T_0 is the initial temperature, α_i is the linear thermal expansion coefficient of the i-th structure and $H(x)$ is the function defined as follows:

$$H(x) = \begin{cases} 1 & for\ x > 0 \\ 0{,}5 & for\ x = 0 \\ 0 & for\ x < 0 \end{cases} \tag{28}$$

During cooling, the total strain (similarly as during heating) is the sum of strains associated with thermal expansion (in this case, the shrinkage of the material) as well as structural strains. Volumetric increase can be attributed to the high density of austenite (highest among the hardening structures such as martensite, bainite, ferrite and pearlite). The strain caused during cooling can be described by the following relation [44]:

$$\varepsilon^{C} = \varepsilon^{Tc} + \varepsilon^{Trc} \tag{29}$$

where ε^{Tc} is the strain caused by thermal shrinkage of material:

$$\begin{aligned}\varepsilon^{Tc} = & \alpha_A (T - T_{SOL}) H(T - T_s) + \alpha_A (T_s - T_{SOL}) H(T_s - T) + \\ & + \sum_{i=A,P,F,B,M} \alpha_i \varphi_i (T - T_{si}) H(T_{si} - T)\end{aligned} \tag{30}$$

while ε^{Trc} is the strain caused by phase transformation during cooling:

$$\varepsilon^{Trc} = \sum_{i=P,F,B,M} \varphi_i \gamma_{Ai} \tag{31}$$

where T_{SOL} denotes solidus temperature, T_s the initial temperature of phase transformation, T_{si} the initial temperature of austenite transformation in the i-th structure and γ_{Ai} the structural strain of austenite in the i-th structure. In addition, due to the limitation of the existence of solid state material:

$$\varepsilon(x,y,z,t) = 0 \quad for \quad T > T_{SOL} \tag{32}$$

5. The example of calculation of temperature field and phase transformations in welded flats

In the considered example, it is assumed that the welded material is steel S235 with the following material constants: specific heat C_p = 670 J/(kg·K), density ρ = 7800 kg/m^3, thermal diffusivity $a = 1.2 \times 10^{-5}$ m^2/s, the temperatures at the beginning and end of austenite transformation, respectively, A_1 = 996 K (723°C) and A_3 = 1108K (835°C), solidus temperature T_S = 1763K (1490°C) and the liquidus temperature T_L = 1793K (1520°C). The model of joining two butt-welded flats with a thickness of 0.012 m and a width of 0.1 m is shown in **Figure 5**.

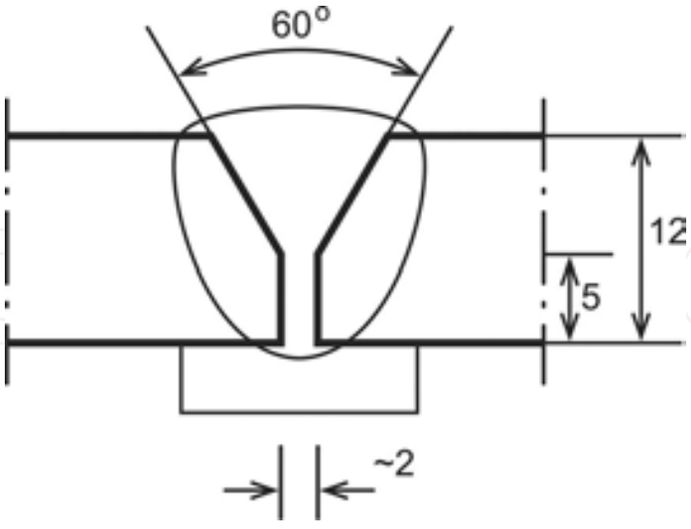

Figure 5. Scheme of the welded joint with technology chamfering.

The speed and power of the movement source are assumed to be v = 0.005 m/s and P = 18000 W, respectively. Time-varying temperature field was determined according to the formulas (Eqs. (11)–(15)). The temperature field on the upper surface of the welded flats and in the

http://dx.doi.org/10.5772/63994

longitudinal section determined by the trace of the source transition is shown in **Figures 6** and **7**.

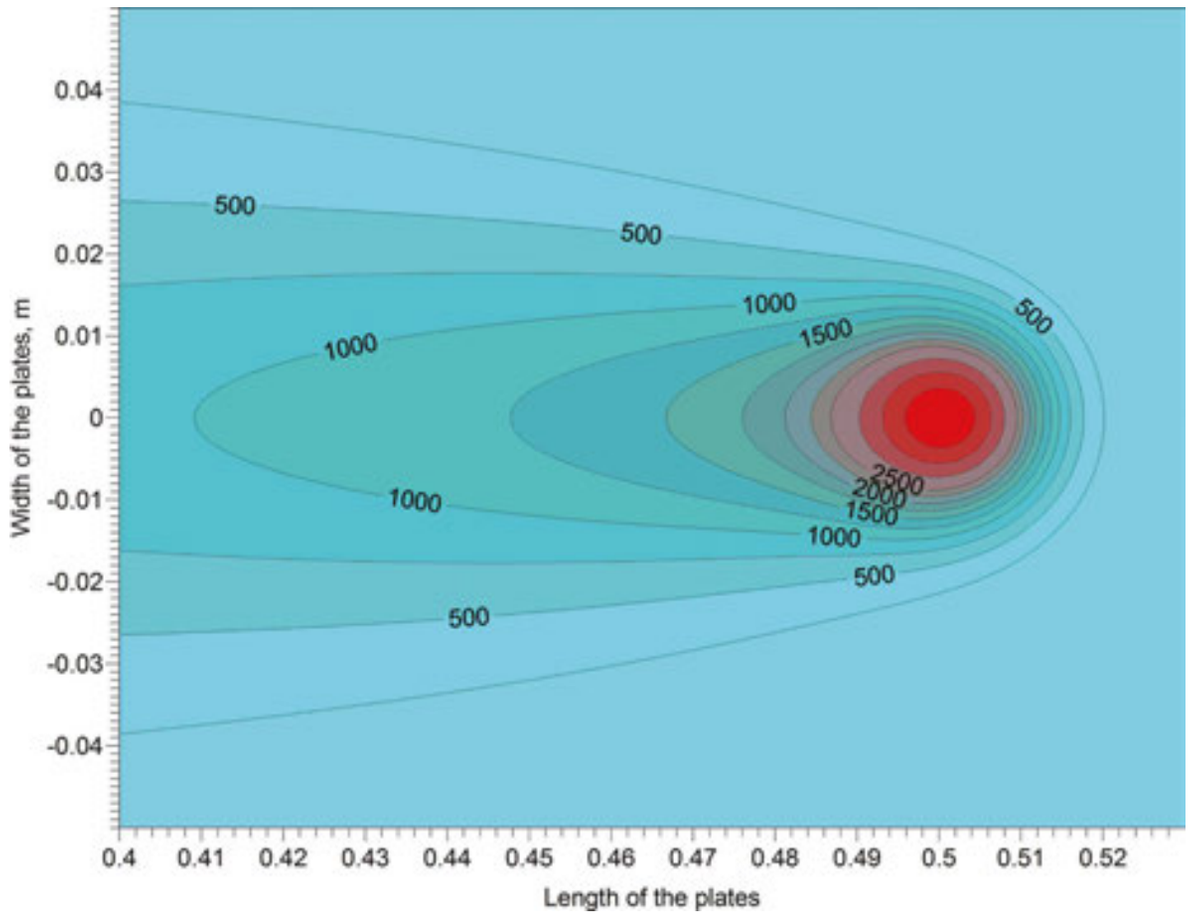

Figure 6. Temperature distribution (°C) on the surface of flats at time t = 102 s from beginning of welding.

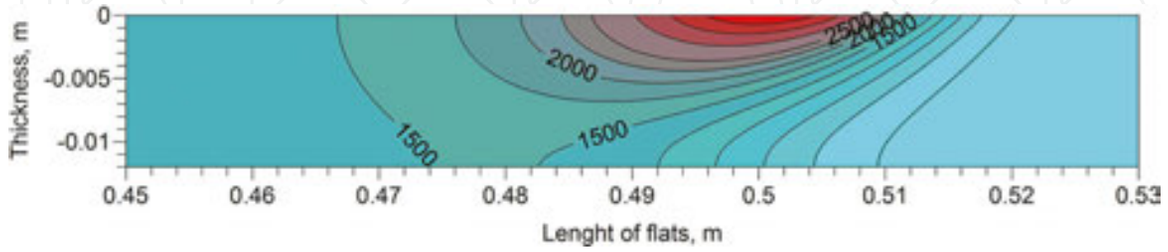

Figure 7. Temperature distribution (°C) in longitudinal section at time t = 102 s from beginning of welding.

The quantities $B_1 = B_2 = B$ are considered in calculations, which are equal to the width of one flat, thereby obtaining a temperature field symmetrical to the plane defined by vertical axis of

the source and the direction of its movement. Thus, both this and the further calculation illustrations are shown on the right symmetrical cross-section which is perpendicular to a moving heat source. The image of maximum temperature isotherms in a cross-section of the joint (on the front contact of flats) is shown in **Figure 8**.

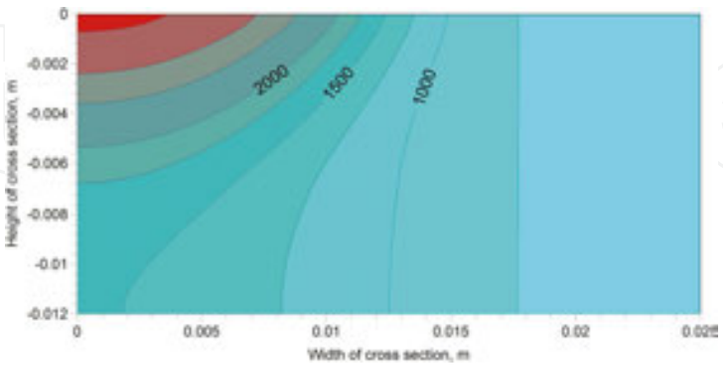

Figure 8. Maximum temperatures (°C) in half of cross-section of welded flats.

On the basis of the maximum temperature field achieved in particular areas of the weld joint, specific heat-affected zones were determined (**Figure 9**) specified by limit temperatures T_L, T_S, A_3 and A_1. The weld area is limited by a liquidus isotherm, which implies covering the part of the section wherein complete melting of the material occurred. Incomplete melting is limited by both liquidus and solidus temperatures. The heat-affected zone is determined by solidus isotherms and A_1. In addition, in the region between the solidus and A_3 temperatures, ferrite and pearlite, the starting components of steel, have been completely transformed into austenite, whereas in the temperature range A_1-A_3, there is an incomplete conversion. In the area where the temperature did not exceed A_1, certainly, phase transitions did not occur and the structure of the parent material (ferritic-pearlitic) was thus preserved. The participation of the heating structures was determined on the basis of the Fe-C diagram. The participation of the cooling structure was determined on the basis of knowledge of the TTT-welding diagram for welding steel S235 and the variations in temperature during cooling (**Figure 10**) [45].

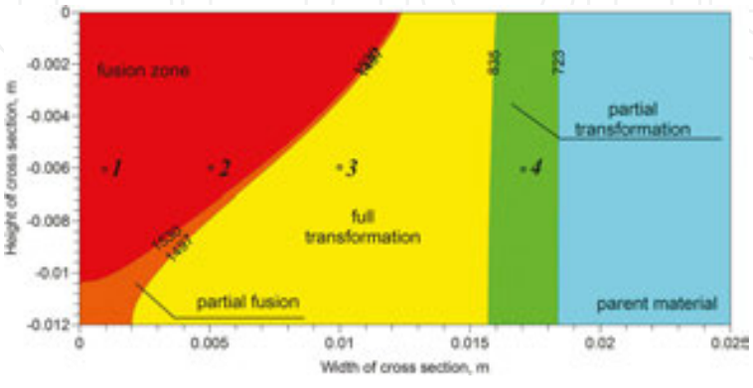

Figure 9. Heat-affected zones (HAZ) with selected points.

http://dx.doi.org/10.5772/63994

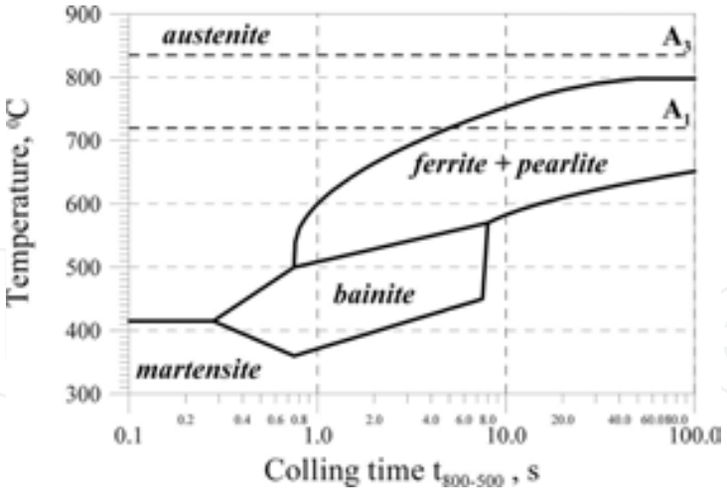

Figure 10. TTT-welding diagram for S235 steel.

The analysis of the cooling speed $v_{8/5}$ showed that after complete cooling in both weld and heat-affected zone, wherein there has been complete and partial transformation of ferrite and pearlite into austenite, supercooled austenite resulted in a ferrite-pearlite structure. Changes in the temperature and structure in the considered cross-section for the selected time of the welding cycle are shown in **Figures 11–19**. The analysis of these changes was investigated on a symmetrical half of the cross-section of the flats' connection, which is perpendicular to the direction of source movement and $x_0 = 0.5$ m from the beginning of the flats (in half their length), that is, from the beginning of the coordinate system associated with flats. For $t = 0$, the beginning of the coordinate systems associated with the source and the welded object overlaps. **Figures 11–13** illustrate the condition where the joint area was completely filled with the welded material, there were no cooling phase transitions and the largest participation of austenite is observed. By contrast, **Figures 14–19** illustrate the gradual decrease in the share of austenite which forms a ferritic-pearlitic structure following the temperature drop.

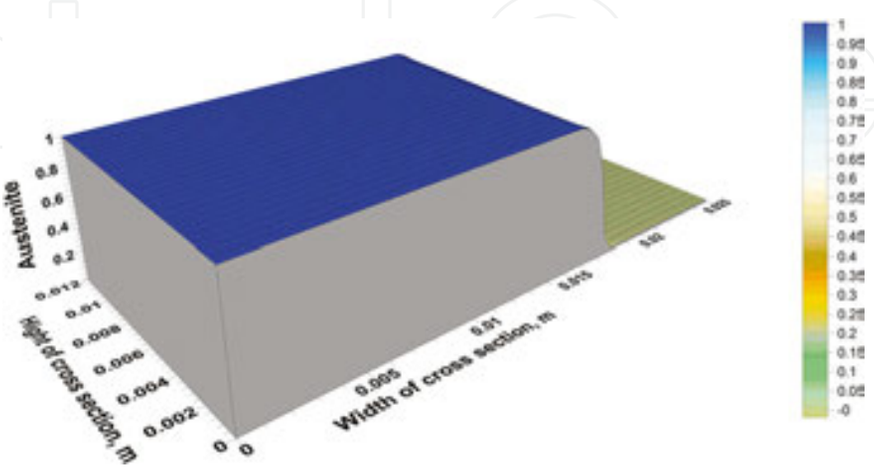

Figure 11. Volume fraction of austenite in cross-section at time $t = 109$ s from process beginning.

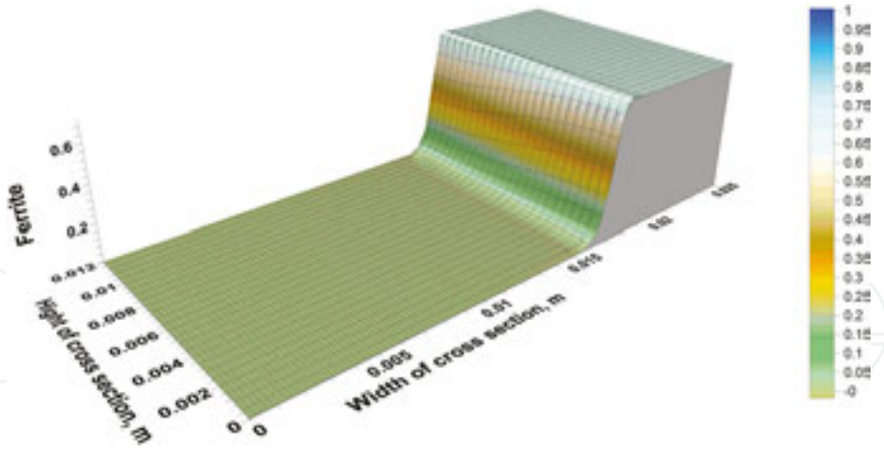

Figure 12. Volume fraction of ferrite in cross-section at time t = 109 s from process beginning.

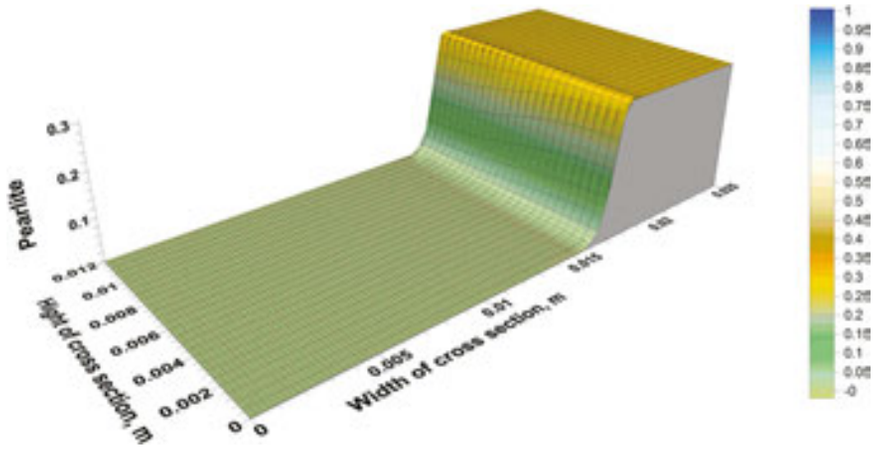

Figure 13. Volume fraction of pearlite in cross-section at time t = 109 s from process beginning.

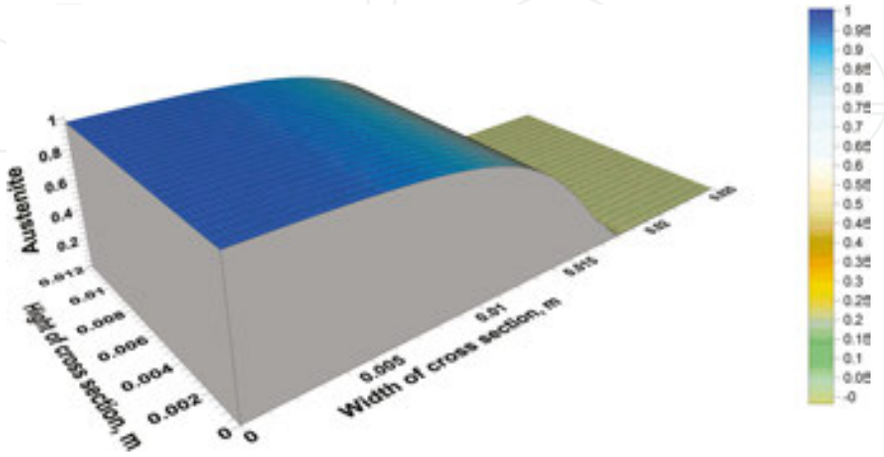

Figure 14. Volume fraction of austenite in cross-section at time t = 134 s from process beginning.

http://dx.doi.org/10.5772/63994

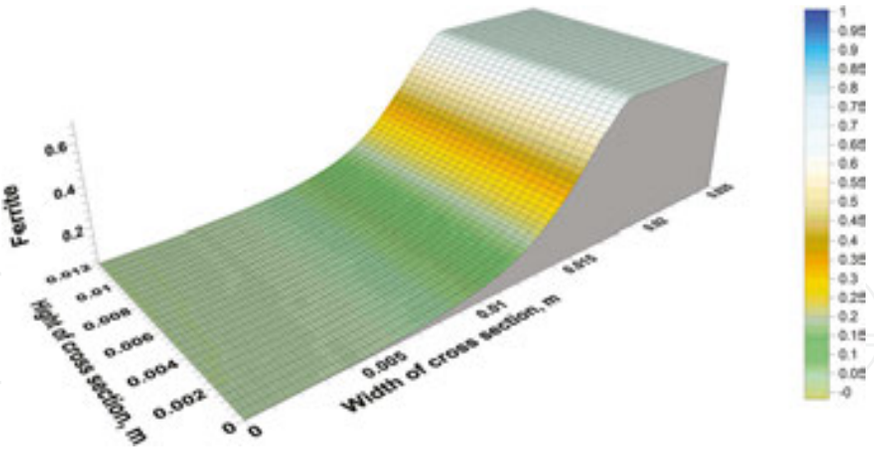

Figure 15. Volume fraction of ferrite in cross-section at time t = 134 s from process beginning.

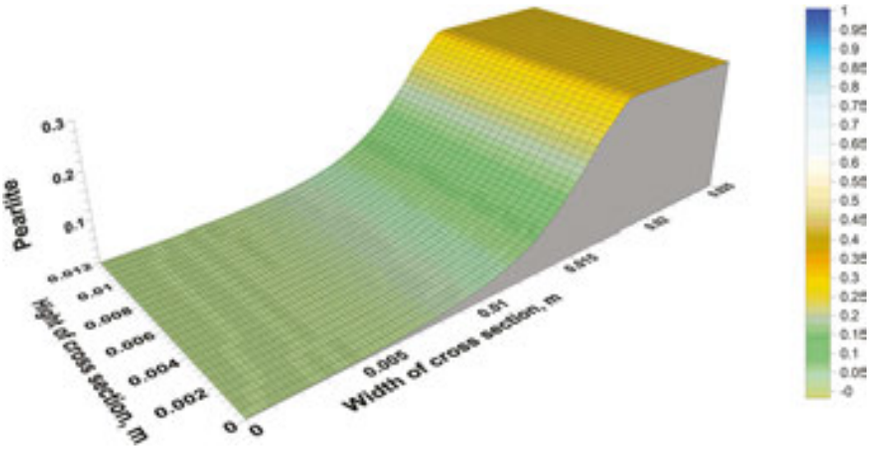

Figure 16. Volume fraction of pearlite in cross-section at time t = 134 s from process beginning.

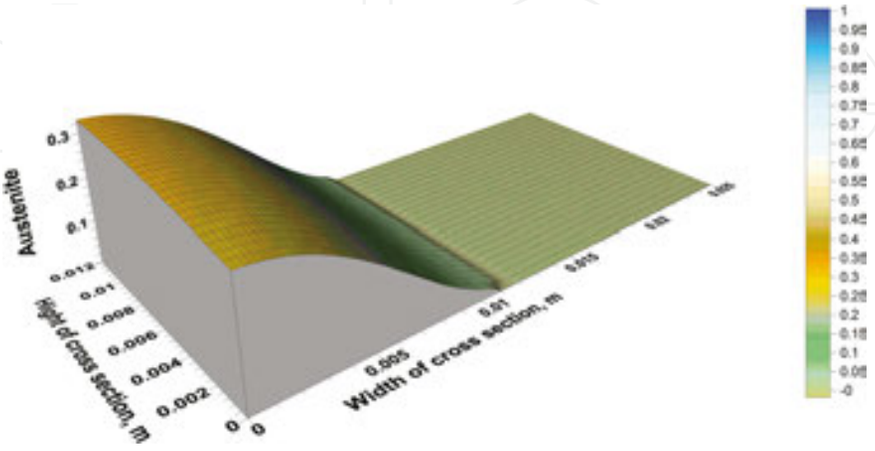

Figure 17. Volume fraction of austenite in cross-section at time t = 146 s from process beginning.

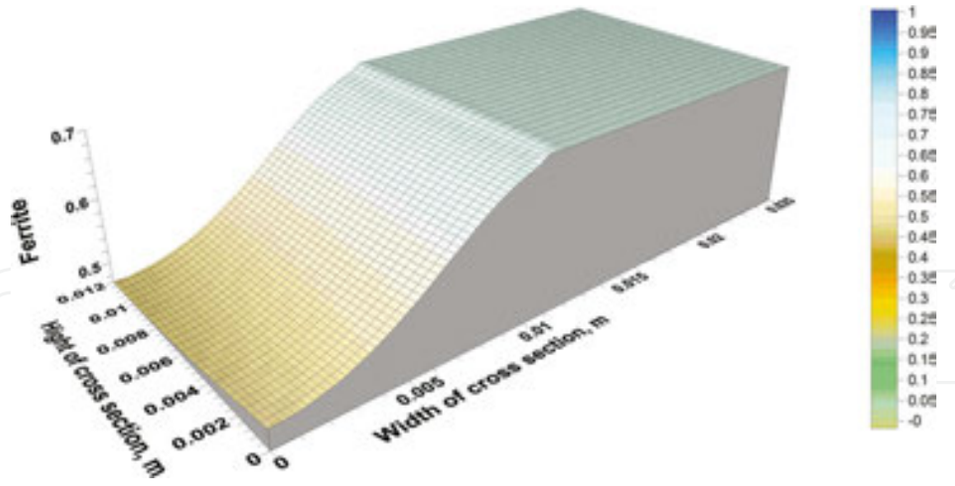

Figure 18. Volume fraction of ferrite in cross-section at time t = 146 s from process beginning.

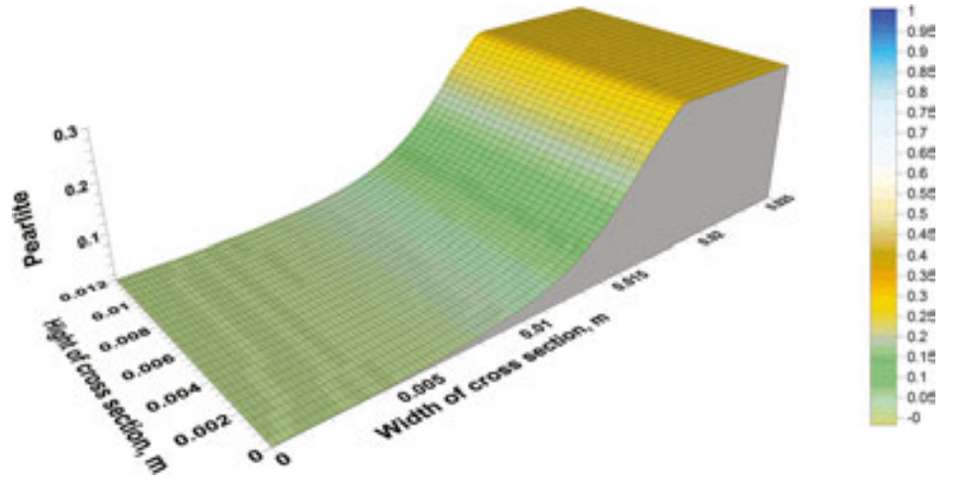

Figure 19. Volume fraction of pearlite in cross-section at time t = 146 s from process beginning.

Changes in temperature and volume fraction of the individual structural components at the selected points in the cross-section (comp. **Figure 9**) are shown in **Figure 20**.

Point *1* is located in the area of chamfering of flats; hence, the graph of temperature and austenite volume fraction starts at the moment of the joint execution. At points *2* (fusion zone) and *3* (full-transformation zone), a complete austenite transformation occurs. But at point *2*, apart from phase transformations in the solid state, melting and solidification phase transformations occur, resulting in a diverse dendritic structure shown during metallographic testing. At point 4, a partial transformation of the primary structure into austenite occurs, which is visible on the graph.

In strain calculations, linear expansion coefficients of the particular structural elements were assumed and structural stresses (**Table 1**) were determined on the basis of the author's own dilatometric research [46].

http://dx.doi.org/10.5772/63994

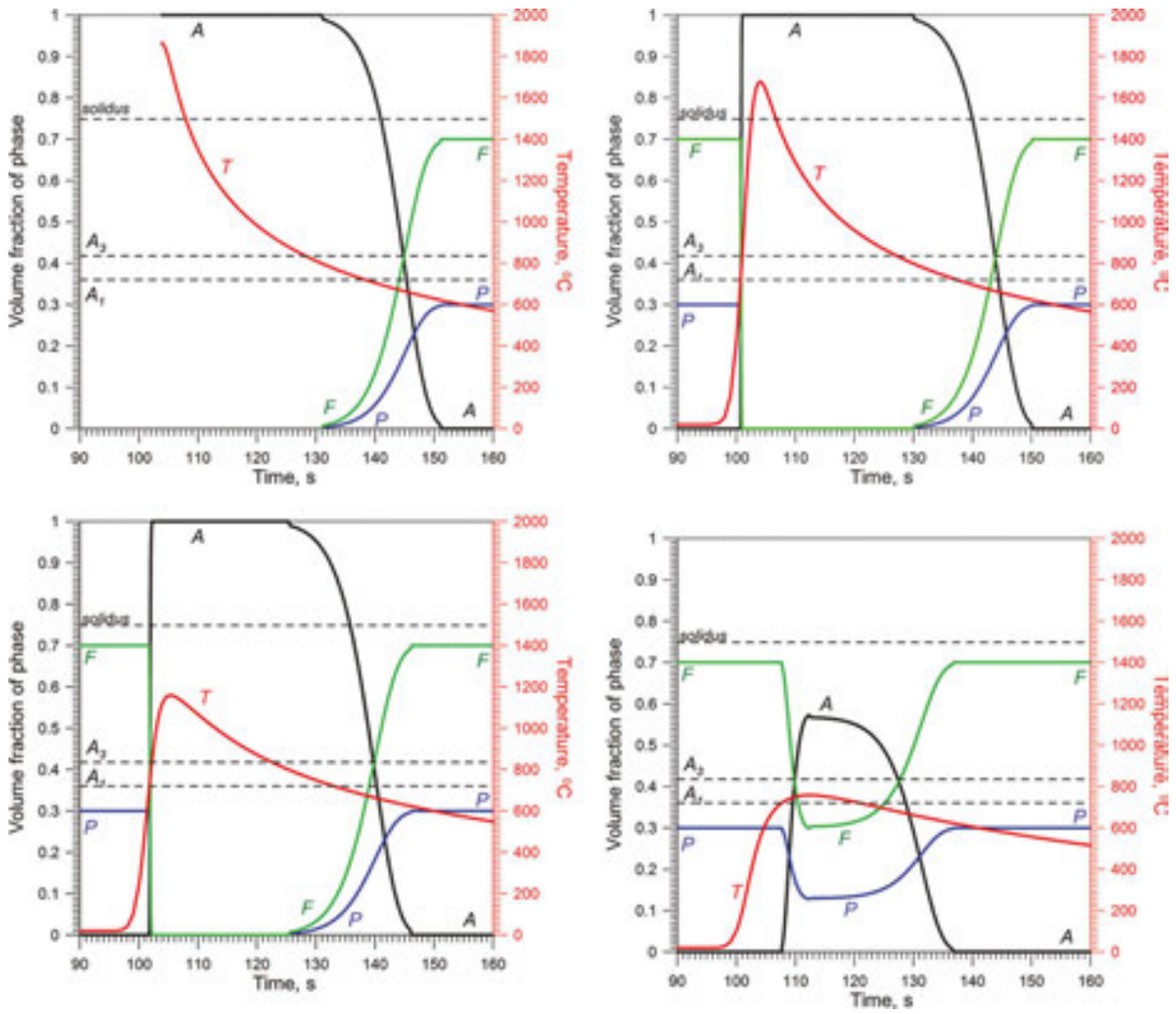

Figure 20. Welding thermal cycles and volume fractions of phases at selected points: T—temperature, A—austenite, P—pearlite, F—ferrite.

	α [1/°C]		γ
Austenite	2.178×10^{-5}	$\gamma_{F,P,S\rightarrow A}$	1.986×10^{-3}
Ferrite	1.534×10^{-5}	$\gamma_{B\rightarrow A}$	1.440×10^{-3}
Pearlite	1.534×10^{-5}	$\gamma_{A\rightarrow F,P}$	3.055×10^{-3}
Bainite	1.171×10^{-5}	$\gamma_{A\rightarrow B}$	4.0×10^{-3}
Martensite	1.36×10^{-5}		

Table 1. Structural (γ) and thermal (α) expansion coefficients of phases.

Dilatometric graphs (thermal and structural strains as a function of temperature) for selected points of the section (comp. **Figure 9**) are shown in **Figure 21**. In **Figure 21a**, a dilatometric graph for point *1* of the weld area is presented, where the material is deposited in the liquid phase as the molten material of the electrode, flux and partially melted edges of the flats; therefore, we observe only shrinkage "negative" strains of the cooling metal with a clear fault

reflecting the strain of austenite transformation into ferrite and pearlite. Point *2* (**Figure 21b**) is located in the area of melting of the starting material, and the dashed line in the figure reflects the change of state from solid to liquid. The solid line (bottom) is initiated by weld solidification.

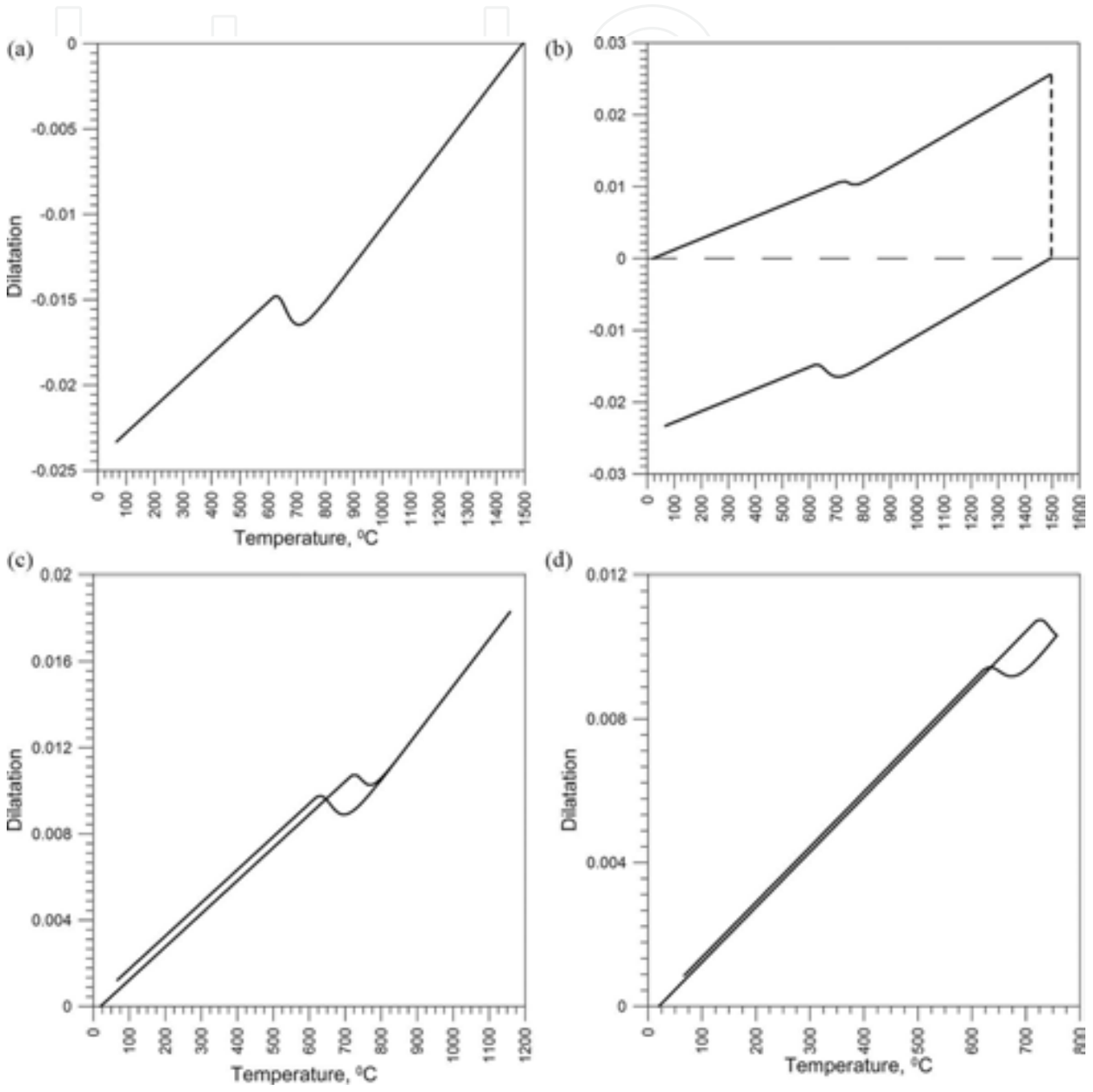

Figure 21. Dilatometric curves for selected points of cross-section.

Dilatometric graph in point *3* (**Figure 21c**) illustrates the history of strain changes for a full thermal cycle. In the considered point, the material with a ferritic-pearlitic structure is completely transformed into austenite during heating (lower line), which is shown with a fault in the diagram in the temperature range 723–835°C. At point 4 (**Figure 21d**) partial conversion

http://dx.doi.org/10.5772/63994

of ferrite and pearlite in austenite was observed, that is, at that point, the temperature during heating has exceeded the temperature of the beginning of austenitizing A_1, but has not reached the final temperature of austenitizing A_3. The stage of the austenite transformation is determined linearly in a numerical model by making the austenite transformation progress conditionally on the ratio $(T_{max} - A_1)/(A_3 - A_1)$, where T_{max} is the maximum temperature reached at a particular point of the weld joint.

6. Verification of the results of numerical simulation of phase transitions with the results of metallographic research

In order to verify the results of the numerical calculations, metallographic tests of the butt-welded joint were carried out. For this purpose, two flats with identical geometry as calculated, that is, two flats with a thickness of 0.012 m and width of 0.1 m, were welded. The material of the flats was steel S235. Before making the joint, sheet chamfering was conducted. Then, welding was carried out with the submerged arc welding method, under welding flux Taste-3 and with SPGΦ15 wire. Welding parameters were voltage U = 30 V, current I = 600 A and welding speed 20 m/h. The diagram of the elements prepared for joining is presented in **Figure 5** (identical to the welded joint adopted for numerical analysis). Cross-section of the weld joint (the image of the sample taken for metallographic examinations) is presented in **Figure 22**. Metallographic analysis was performed for specific zones of a welded joint, that is, for the area of weld, heat-affected zone and parent material. **Figure 23** shows an image of the middle part of the welded joint (at the junction of welded flats) with a clearly visible dendritic structure which is characteristic of solidification. **Figure 24** shows an image of the structure in the right symmetrical part of the welded joint in the area from the weld to the ferrite-pearlite structure of the parent material. On the border of the weld, dendrites are visible, which change in the heat-affected zone into a structure with the Widmannstatten structure elements.

Figure 22. Cross-section of a welded joint: sample taken for metallographic analysis, magnification 2×.

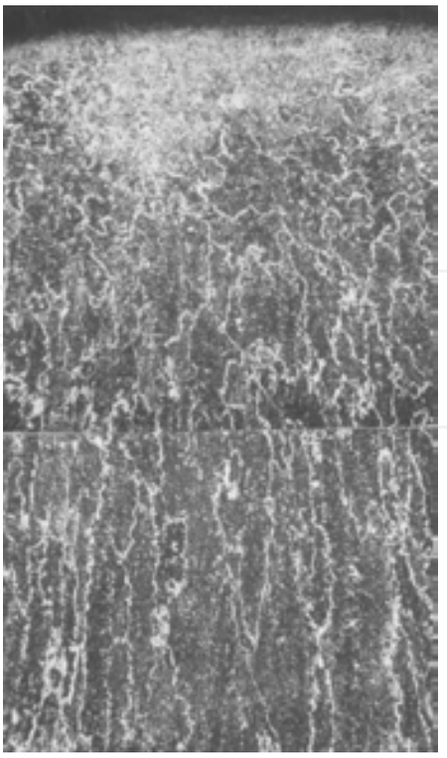

Figure 23. Weld, magnification 140×.

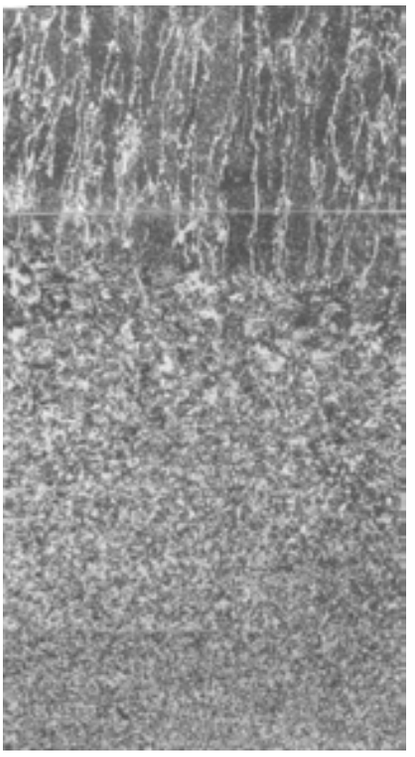

Figure 24. Transition zone, magnification 140×.

http://dx.doi.org/10.5772/63994

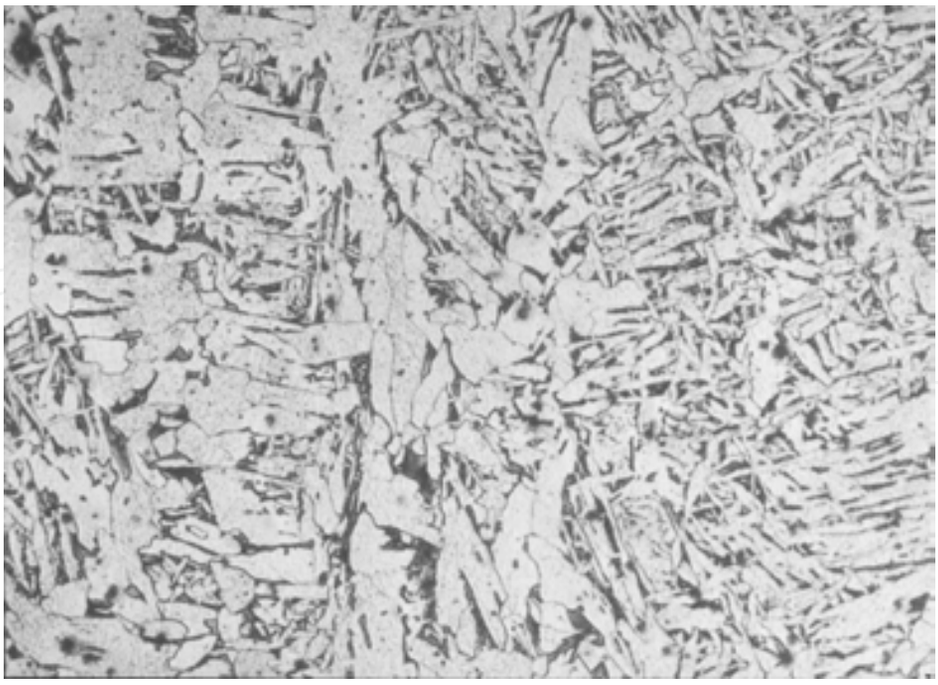

Figure 25. Weld, Nital Etch, magnification 250×, ferritic-pearlitic dendritic structure.

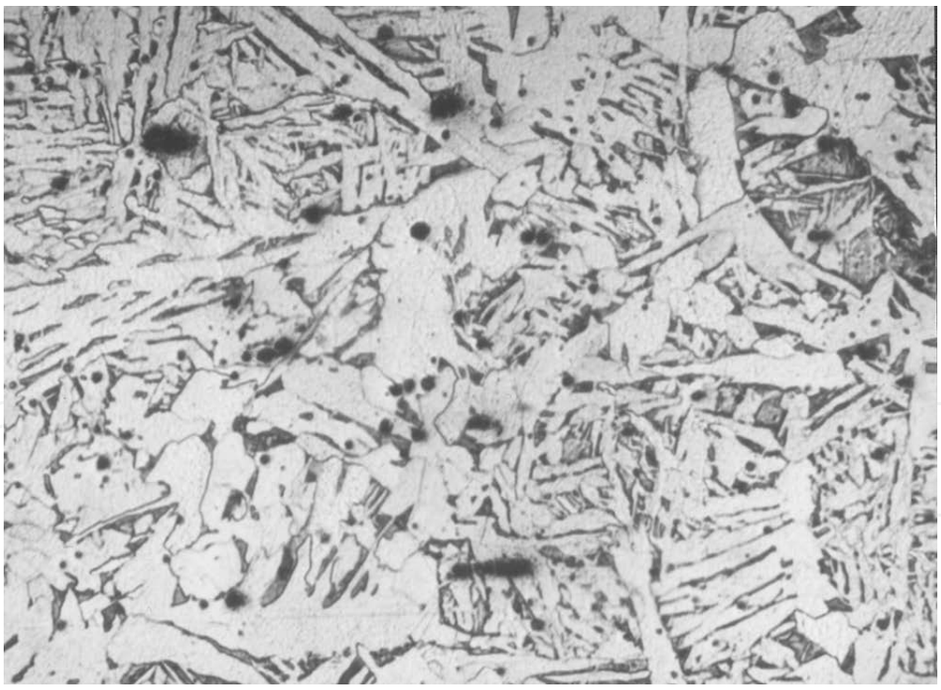

Figure 26. Heat affected zone, Nital Etch, magnification 250×, ferritic-pearlitic structure.

Next, the images of structures of individual areas are presented. In the area of the weld (**Figure 25**), we observe the ferritic-pearlitic structure with a small amount of supercooled pearlite and island bainite in the dendritic system characteristic of solidified structures. In the

heat-affected zone (**Figure 26**), ferrite, pearlite and pearlite balls supercooled with a number of non-metallic inclusions are visible. Primary structure of the parent material (**Figure 27**) consists of ferrite and pearlite in the band system (hardly visible).

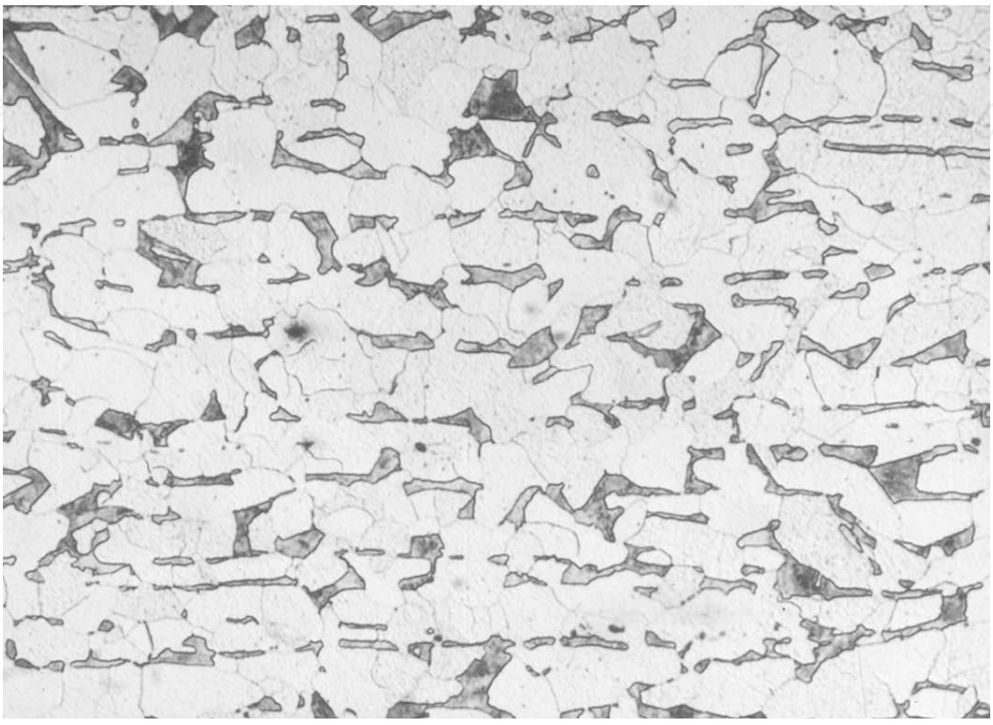

Figure 27. Parent material, Nital Etch, magnification 250×, ferritic-pearlitic banded structure.

The results of metallographic tests show high conformity with the results of numerical simulation and testify to the correctness of the developed numerical model.

7. Conclusion

The proposed model for determining temperature field allows to obtain characteristic zones of the weld joint with shapes and dimensions similar to the real ones. Metallographic verification of the results of numerical simulation of phase transitions also provided satisfactory results.

Analysis of phase transformations occurring during the welding process allowed determination of the quantitative composition of the cooling structures in the weld area (in the heat-affected zone).

This approach allows for an accurate tracking of changes in phase participations and the course of thermal and phase strains, which enable to determine, within the framework of thermoplasticity theory, welding stresses temporary and residual welding stresses.

Author details

Jerzy Winczek

Address all correspondence to: winczek@gmail.com

Czestochowa University of Technology, Czestochowa, Poland

References

[1] Rosenthal D. Mathematical theory of heat distribution during welding and cutting. Welding J. 1941;20:220s–234s

[2] Rykalin N N. Fundamentals of heat flow in welding. AN SSSR: Moskva;1947. 272 p.

[3] Eagar T W, Tsai N S. Temperature fields produced by traveling distributed heat sources. Welding J. 1983;62:346s–355s

[4] Goldak J, Chakravarti A, Bibby M. A new finite element model for welding heat sources. Metall Trans. 1984;15B:299–305

[5] Bo K S, Cho H S. Transient temperature distribution in arc welding of finite thickness plates. Proc Inst Mech Eng. 1990;204B3:175–183

[6] Radaj D. Heat effects of welding. Temperature field, residual stress, distortion, Springer-Verlag; Berlin Heidelberg. 1992; 348 p.

[7] Jeong S K, Cho H S. An analytical solution to predict the transient temperature distribution in fillet arc welds. Welding J. 1997;76:223s–232s

[8] Nguyen N T, Mai Y W, Simpson S, Ohta A. Analytical approximate solution for double ellipsoidal heat source in finite thick plate. Welding J. 2004;84:82s–93s

[9] Kwon Y, Weckman D C. Analytical thermal model of conduction mode double sided arc welding. Sci Technol Weld Join. 2008;13:539–549

[10] Fachinotti V D, Anca A A, Cardona A. Analytical solutions of the thermal field induced by moving double-ellipsoidal and double elliptical heat sources in a semi-infinite body. Int J Num Meth Biomech Eng. 2011;27:595–607

[11] Antonakakis T, Maglioni C, Vlachoudis V. Closed form solutions of the heat diffusion equation with Gaussian source. Int J Heat Mass Transf. 2013;62:314–322

[12] Ghosh A, Barman N, Chattopadhyay H, Hloch S. A study of thermal behaviour during submerged arc welding. Strojniški vestnik – Journal of Mechanical Engineering. 2013;59:333–338

[13] Franko A, Romoli L, Musacchio A. Modelling for predicting seam geometry in laser beam welding of stainless steel. Int J Thermal Sci. 2014;79:194–205

[14] Salimi S, Bahemmat P, Haghpanahi M. A 3D transient analytical solution to the temperature field during dissimilar welding processes. Int J Mechn Sci, 2014;79:66–74

[15] Na S J, Lee S Y. A study on the tree- dimensional analysis of the transient temperature distribution in gas tungsten arc welding. Proc Inst Mech Eng. 1987;201B3:149–156

[16] Radaj D. Finite element analysis of welding residual stress. International Conference on Residual Stresses 2, Nancy 1988, Nov. 23–25, Elsevier Applied Science, London. 1989; p. 510–516

[17] Karlsson R I, Josefson B L. Three dimensional finite element analysis of temperatures and stresses in a single – pass butt-welded pipe. Trans ASME. 1990;112:76–84

[18] Mundra K, DebRoy T, Kelkar K M. Numerical prediction of fluid flow and heat transfer in welding with a moving heat source. Num Heat Transf. 1996;29A:115–129

[19] Komanduri R, Hou Z B. Thermal analysis of the arc welding process: part I. General solutions. Metall Mater Trans. 2000;31B:1353–1370

[20] Mahapatra M M, Datta G L, Pradhan B. Three-dimensional finite element analysis to predict the effects of shielded metal arc welding process parameters on temperature distributions and weldment zones in butt and one-sided fillet welds. Proc I Mech – J Eng Manuf. 2006;220:837–845

[21] Kumar A, DebRoy T. Heat transfer and fluid flow during gas-metal-arc fillet welding for various joint configurations and welding positions. Metall Mater Trans. 2007;38A: 506–519

[22] Wang S, Goldak J, Zhou J, Tchernov S, Downey D. Simulation on the thermal cycle of a welding process by space-time convection-diffusion finite element analysis. Int J Thermal Sci. 2009;48:936–947

[23] Lindgren L E. Finite element modeling and simulation of welding. Part 1: increased complexity. J Thermal Stresses. 2001;24:141–192

[24] Hongyuan F, Qingguo M, Wenli X, Shude J. New general double ellipsoid heat source model. Sci Tech Weld Join. 2005;10:361–368

[25] Deng D. FEM prediction of welding residual stress and distortion in carbon steel considering phase transformation effects. Mater Dsgn. 2009;30:359–366

[26] Jiang W, Liu Z, Gong J M, Tu S T. Numerical simulation to study the effect of repair width on residual stresses of stainless steel clad plate. Int J Pres Ves Pip. 2010;87:457–463

[27] Lee H T, Chen C T, Wu J L. 3D numerical study of effects of temperature field on sensitisation of Alloy 690 butt welds fabricated by gas tungsten arc welding and laser beam welding. Sci Tech Weld Join. 2010;15:605–612

[28] Joshi S, Hildebrand J, Aloraier A S, Rabczuk T. Characterization of material properties and heat source parameters in welding simulation of two overlapping beads on a substrate plate. Comp Mater Sci. 2013;69:559–565

[29] Fu G, Lourenco M I, Duan M, Estefen S F. Effect of boundary conditions on residual stress and distortion in T-joint welds. J Constr Steel Res. 2014;02:121–135

[30] Chen Y, He Y, Chen H, Zhang H, Chen S. Effect of weave frequency and amplitude on temperature field in weaving welding process. Int J Adv Manuf Techn. 2014;75:803–813

[31] Tsai N S, Eagar T W. Distribution of the heat and current fluxes in gas tungsten arc. Metall Trans. 1985;16B:841–846

[32] Piekarska W, Kubiak M. Three-dimensional model for numerical analysis of thermal phenomena in laser-arc hybrid welding process. Int J Heat Mass Transf. 2011;54:4966–4974

[33] Chen J, Schwenk C, Wu C S, Rethmeier M. Predicting the influence angle on heat transfer and fluid flow for new gas metal arc processes. Int J Heat Mass Transf. 2012;55:102–111

[34] Geissler E., Bergmann H W. Calculation of temperature profiles heating and quenching rates during laser processing. Optoelektronik Magazin. 1987;3:430–434

[35] Geissler E., Bergmann H W. 3D Temperature fields in laser transformation hardening, part I: quasi-stationary fields. Optoelektronik Magazin. 1988;4:396–403

[36] Carslaw H S, Jaeger J C. Conduction of heat in solids. Clarendon Press: London 1996.

[37] Ruge J. Handbook of welding technology, vol. 1: Materials. Springer Verlag;Berlin:1980

[38] Rhode J, Jeppson A. Literature review of heat treatment simulations with respect to phase transformation, residual stresses and distortion. Scand J Metall. 2000;29:47–62

[39] Piekarska W, Kubiak M, Bokota A. Numerical simulation of thermal phenomena and phase transformations in laser-arc hybrid welded joint. Archiv Metall Materials. 2011;56:409–421

[40] Avrami M. Kinetics of phase change. I. General theory. J Chem Physics. 1939;7:1103–1112

[41] Parkitny R, Winczek J. Modelling of phase transformations during multipass surfacing, In: Conf. Proc. XXXVIII Sympozjon Modelling in Mechanics, Silesian University of Technology, Gliwice. 1999; p. 219–224

[42] Koistinen D P, Marburger R E. A general equation prescribing the extent of the austenite-martensite transformation in pure iron-carbon alloys and plain carbon steels. Acta Metall. 1959;7:59–60

[43] Domański T, Bokota A. Numerical models of hardening phenomena of tools steel base on the TTT and CCT diagrams. Archiv Metall Mater. 2011;56:325–344

[44] Winczek J. A simplified method of predicting stresses in surfaced steel rods, J Mater Proces Technol, 2012;212:1080–1088

[45] Brózda J, Pilarczyk J, Zeman M. TTT-welding diagrams transformation of austenite. Śląsk; Katowice. 1983; 139 p.

[46] Winczek J, Kulawik A. Dilatometric and hardness analysis of C45 steel tempering with different heating-up rates. Metalurgija. 2012;51(1):9–12